Real-time time-dependent density functional theory implementation of electronic circular dichroism applied to nanoscale metal-organic clusters

The Journal of Chemical Physics

Real-time time-dependent density functional theory implementation of electronic circular dichroism applied to nanoscale metal–organic clusters

Cite as: J. Chem. Phys. **154**, 114102 (2021); https://doi.org/10.1063/5.0038904
Submitted: 27 November 2020 . Accepted: 25 February 2021 . Published Online: 15 March 2021

Esko Makkonen, Tuomas P. Rossi, Ask Hjorth Larsen, Olga Lopez-Acevedo, Patrick Rinke, Mikael Kuisma, and Xi Chen

AIP Publishing

The Journal of Chemical Physics ARTICLE scitation.org/journal/jcp

Real-time time-dependent density functional theory implementation of electronic circular dichroism applied to nanoscale metal–organic clusters

Cite as: J. Chem. Phys. 154, 114102 (2021); doi: 10.1063/5.0038904
Submitted: 27 November 2020 • Accepted: 25 February 2021 •
Published Online: 15 March 2021

Esko Makkonen,[1] Tuomas P. Rossi,[1,2,a)] Ask Hjorth Larsen,[3] Olga Lopez-Acevedo,[4] Patrick Rinke,[1] Mikael Kuisma,[5,a)] and Xi Chen[1,a)]

AFFILIATIONS

[1]Department of Applied Physics, Aalto University, Espoo, Finland
[2]Department of Physics, Chalmers University of Technology, Gothenburg, Sweden
[3]Simune Atomistics S.L., Donostia-San Sebastián, Spain
[4]Instituto de Física, Facultad de Ciencias Exactas y Naturales, Universidad de Antioquia, Medellín, Colombia
[5]Nanoscience Center, University of Jyväskylä, Jyväskylä, Finland

[a)]**Authors to whom correspondence should be addressed:** tuomas.rossi@aalto.fi; mikael.kuisma@jyu.fi; and xi.6.chen@aalto.fi

ABSTRACT

Electronic circular dichroism (ECD) is a powerful spectroscopy method for investigating chiral properties at the molecular level. ECD calculations with the commonly used linear-response time-dependent density functional theory (LR-TDDFT) framework can be prohibitively costly for large systems. To alleviate this problem, we present here an ECD implementation within the projector augmented-wave method in a real-time-propagation TDDFT framework in the open-source GPAW code. Our implementation supports both local atomic basis sets and real-space finite-difference representations of wave functions. We benchmark our implementation against an existing LR-TDDFT implementation in GPAW for small chiral molecules. We then demonstrate the efficiency of our local atomic basis set implementation for a large hybrid nanocluster and discuss the chiroptical properties of the cluster.

I. INTRODUCTION

Chirality is an essential property in several branches of science and technology. Chiral molecules play a fundamental role in biological activities;[1] for example, DNA double-helices are right-handed and amino acids are left-handed. Chirality is also critical in pharmaceuticals. For example, *R*-enantiomer thalidomide is effective against morning sickness for pregnant women, but the *S*-species produce fetal deformations.[2,3] In addition, chiral molecules and chiral nanomaterials have many potential applications in catalysis, sensors, spintronics, optoelectronics, and nanoelectronics.[4–13] Therefore, the determination of the handedness of chiral systems is of paramount importance.

Chiral molecules absorb left and right circular polarizations of light differently. This difference is probed in electronic circular dichroism (ECD) spectroscopy. ECD is defined as $\Delta\epsilon = \epsilon_L - \epsilon_R$, where ϵ_L and ϵ_R are the molar extinction coefficients for left and right circularly polarized light, respectively. Since ECD is highly sensitive to small details in the atomic structure of molecules and unique for each conformation, it is a powerful technique for characterizing chiral systems and for distinguishing enantiomers.[14]

ECD spectroscopy accompanied by computational modeling provides insightful knowledge of the atomic structures of chiral biomolecules and nanoclusters.[15–17] For example, in our earlier work, we have identified by comparing simulated and measured ECD that the Ag^+-mediated guanine duplex has the left-handed helix configuration,[16] while the Ag^+-mediated cytosine has the right-handed helix configuration.[17]

Most computational ECD approaches are based on the linear-response formalism.[18] Time-dependent density-functional theory (TDDFT)[19] has become the linear-response method of choice due to its favorable balance of accuracy and computational cost, compared to quantum chemical approaches such as coupled cluster and configuration interaction methods.[18,20,21] In linear-response TDDFT (LR-TDDFT), the Casida equation[22,23] is solved in the basis of Kohn–Sham (KS) particle–hole transitions in the frequency domain.[24,25] A full ECD spectrum requires the calculation of a large number of transitions from occupied to unoccupied states. This becomes computationally prohibitive for large systems with a high density of states.

An alternative to LR-TDDFT is real-time-propagation time-dependent density-functional theory (RT-TDDFT). In RT-TDDFT, the system is subjected to an initial perturbation and the KS wave functions are propagated in the time domain by numerically integrating the time-dependent KS equations. The real-time approach captures the same information as LR-TDDFT for small initial perturbations and incorporates nonlinear spectral information for larger initial perturbations.[23,26–28]

RT-TDDFT scales better with the system size than LR-TDDFT but suffers from a large prefactor. LR-TDDFT is usually faster for small systems such as small organic molecules. For large molecules, clusters, or nanoparticles, RT-TDDFT then becomes often more cost-effective than LR-TDDFT.[23,29]

RT-TDDFT for ECD has been implemented for a variety of basis sets: real-space grids,[27,30] Gaussian-type atomic orbitals,[31] and a mix of Gaussian-type and plane-wave basis sets.[32] Recently, external magnetic fields have also been implemented.[33,34]

In this work, we present a RT-TDDFT ECD implementation in the open-source GPAW package.[35,36] GPAW hosts an efficient RT-TDDFT module[37] with localized basis sets (LCAO mode)[38] within the projector augmented method (PAW),[39] a unique combination suitable for large systems. In addition, the real-space-grid RT-TDDFT module[40] allows efficient benchmarking of basis set calculations. We verify our implementation also by comparing our results to those calculated with the existing LR-TDDFT implementation in GPAW.

In GPAW, the time-dependent density and potential are expressed on a uniform grid, and the matrix elements of the potential are evaluated on this grid.[36] The smoothness of these quantities allows for coarse grid spacing. The LCAO-PAW pseudowave functions can form a local and efficient representation suitable for systems with hundreds of atoms.[38] Previous work has shown that LCAO RT-TDDFT in GPAW is capable of simulating the optical spectrum of a silver cluster of more than 500 atoms (Ag_{561}).[37,41] In this work, we demonstrate the efficiency of our LCAO RT-TDDFT ECD implementation for a large ligand-protected Ag_{78} cluster[42] consisting of over 1000 atoms and over 4000 electrons.

The rest of this paper is organized as follows: In Sec. II, we illustrate the calculation of ECD from the time-dependent magnetic dipole moment, which is calculated with RT-TDDFT in GPAW. The details of all simulations are described in Sec. II C. In Sec. III, we demonstrate the capability of our implementations to predict ECD spectra for four test cases. Finally, we summarize this work in Sec. IV.

II. METHODS

In RT-TDDFT, the KS wave functions are propagated in time in response to a time-dependent potential starting from an initial state, here chosen to be the ground state. The time-dependent KS equation is defined as

$$i\frac{\partial}{\partial t}\psi_n(\mathbf{r},t) = H_{\mathrm{KS}}(t)\Psi_n(\mathbf{r},t), \tag{1}$$

where $H_{\mathrm{KS}}(t)$ is the time-dependent KS Hamiltonian and $\psi_n(\mathbf{r}, t)$ is a time-dependent KS single-particle wave function. A common practice in time-propagation schemes is to use the weak δ-kick approach[26] to calculate the linear-response functions. After perturbing $H_{\mathrm{KS}}(t)$ by the δ-kick at $t = 0$, Eq. (1) is propagated in the present work using the semi-implicit Crank–Nicolson method, the numerical reliability of which has been demonstrated in earlier implementation work.[37,40]

In this work, we implement and benchmark the calculation of the time-dependent magnetic moment within the time-propagation framework for obtaining the ECD spectrum. In the following, we derive the relevant equations within the PAW method.[39]

A. ECD from the induced time-dependent magnetic moment

A commonly used experimental quantity to measure ECD is the difference in molar extinction coefficients $\Delta\epsilon(\omega)$,

$$\Delta\epsilon(\omega) = \frac{16\pi N_{\mathrm{A}}}{3\ln(10)10^3}\frac{2\pi}{\hbar c}\omega R(\omega)^{\mathrm{cgs}}. \tag{2}$$

Here, ω is the energy of the incident light, c is the speed of light, $\hbar$ is the reduced Planck constant, N_{A} is Avogadro's constant, and $R(\omega)^{\mathrm{cgs}}$ is the rotatory strength in cgs units. The quantity that characterizes $\Delta\epsilon(\omega)$ and therefore the ECD spectrum is the rotatory strength. The relationship between rotatory strength in cgs units and rotatory strength in atomic units [denoted as $R(\omega)$] is

$$R(\omega)^{\mathrm{cgs}} = \frac{e^2\hbar^2}{m_e^2\alpha}10^6 R(\omega), \tag{3}$$

where e is the elementary charge, m_e is the mass of an electron, and α is the fine structure constant.[43] We will work in atomic units and perform the required unit conversions afterward.

The equation for rotatory strength is defined through the magnetic dipole moment $m(\omega)$ by

$$R(\omega) = \frac{1}{\pi\kappa}\mathrm{Re}\left[\sum_k m_k^{(k)}(\omega)\right], \tag{4}$$

where index k enumerates Cartesian coordinates ($k \in \{x, y, z\}$). The k superscript in parentheses indicates the δ-kick[26] direction, to be distinguished from the component subscript. We keep the intensity of

the δ-kick, κ, weak to restrict our calculations to the linear-response regime.[26] The derivation of Eq. (4) from the optical response tensor is shown in supplementary material, Note S1. This derivation partly follows the one presented by Varsano *et al.*[30]

In our methodology, $m_j^{(k)}(\omega)$ is calculated by Fourier transform of $m_j^{(k)}(t)$, which has been obtained through time-propagation,

$$m_j^{(k)}(\omega) = \int_0^\infty e^{i\omega t} m_j^{(k)}(t)\, \mathrm{d}t. \tag{5}$$

In principle, the integration interval goes from zero to infinity. In practice, a finite propagation time (T) suffices by introducing an artificial lifetime $\omega \to \omega + i\frac{\sigma^2}{2}t$, where σ is the parameter that determines the linewidth of the Gaussian line shape. Introducing this into Eq. (5) gives

$$m_j^{(k)}(\omega) = \int_0^T e^{i\omega t} e^{-\frac{\sigma^2}{2}t^2} m_j^{(k)}(t)\, \mathrm{d}t. \tag{6}$$

For a desired value of σ, the propagation time T needs to be large enough so that $e^{-\frac{\sigma^2}{2}T^2} \approx 0$.

B. Computing the magnetic moment $m_j^{(k)}(t)$ in the PAW and LCAO formalisms

The magnetic moment is defined by the following operator (in atomic units):

$$\hat{\mathbf{m}} = -\frac{i}{2c}\hat{\mathbf{r}} \times \hat{\nabla}. \tag{7}$$

The expectation value of the time-dependent magnetic moment is obtained as

$$\mathbf{m}(t) = \sum_n f_n \int \psi_n^*(\mathbf{r}, t)\, \hat{\mathbf{m}}\, \psi_n(\mathbf{r}, t)\, \mathrm{d}\mathbf{r}, \tag{8}$$

where f_n is the occupation number of the nth KS orbital and $\psi_n(\mathbf{r}, t)$ is the time-evolved KS one-particle wave function.

In the PAW method,[39] the KS wave functions $\psi_n(\mathbf{r}, t)$ are decomposed as follows:

$$\psi_n(\mathbf{r}, t) = \tilde{\psi}_n(\mathbf{r}, t) + \sum_{ai} \left[\phi_i^a(\mathbf{r}) - \tilde{\phi}_i^a(\mathbf{r})\right] \langle \tilde{p}_i^a | \tilde{\psi}_n(t) \rangle, \tag{9}$$

where $\tilde{\psi}_n(\mathbf{r}, t)$ is a smooth one-particle *pseudowave function* and $\sum_{ai}\left[\phi_i^a(\mathbf{r}) - \tilde{\phi}_i^a(\mathbf{r})\right]\langle \tilde{p}_i^a | \tilde{\psi}_n(t)\rangle$ is a local correction inside an atomic *augmentation sphere*. $\tilde{p}_i^a$ is a localized *projector function* and ϕ_i^a and $\tilde{\phi}_i^a$ are *partial* and *pseudopartial waves*, respectively. These quantities are specific to PAW. In the PAW formalism, the expectation value in Eq. (8) becomes

$$\begin{aligned}\mathbf{m}(t) = &\sum_n f_n \langle \tilde{\psi}_n(t) | \hat{\mathbf{m}} | \tilde{\psi}_n(t) \rangle \\ &+ \sum_{naij} f_n \langle \tilde{\psi}_n(t) | \tilde{p}_i^a \rangle \Delta \mathbf{M}_{ij}^a \langle \tilde{p}_j^a | \tilde{\psi}_n(t) \rangle,\end{aligned} \tag{10}$$

where the augmentation-sphere contribution is $\Delta \mathbf{M}_{ij}^a = \langle \phi_i^a | \hat{\mathbf{m}} | \phi_j^a \rangle - \langle \tilde{\phi}_i^a | \hat{\mathbf{m}} | \tilde{\phi}_j^a \rangle$. For evaluating $\Delta \mathbf{M}_{ij}^a$, the required matrix elements of the form $\langle \phi_i^a | \mathbf{r} \times \nabla | \phi_j^a \rangle$ are evaluated in two atom-centered parts as $\langle \phi_i^a | (\mathbf{r} - \mathbf{R}^a) \times \nabla | \phi_j^a \rangle + \mathbf{R}^a \times \langle \phi_i^a | \nabla | \phi_j^a \rangle$, where $\mathbf{R}^a$ is the coordinate of atom a.

In the LCAO expansion, the time-dependent pseudowave function $\tilde{\psi}_n(\mathbf{r}, t)$ is written as a linear combination of atom-centered basis functions $\varphi_\mu(\mathbf{r} - \mathbf{R}^a)$,

$$\tilde{\psi}_n(\mathbf{r}, t) = \sum_\mu c_{\mu n}(t) \varphi_\mu(\mathbf{r} - \mathbf{R}^a), \tag{11}$$

where $c_{\mu n}(t)$ are the time-dependent expansion coefficients. With this LCAO expansion, Eq. (10) can be written compactly as

$$\mathbf{m}(t) = \sum_{\mu\nu} \rho_{\nu\mu}(t) \mathbf{M}_{\mu\nu}, \tag{12}$$

where $\rho_{\mu\nu}(t) = \sum_n f_n c_{\mu n}(t) c_{\nu n}^*(t)$ is the KS density matrix in the LCAO basis. The matrix elements $\mathbf{M}_{\mu\nu}$ are given by the pseudo- and augmentation contributions,

$$\mathbf{M}_{\mu\nu} = \tilde{\mathbf{M}}_{\mu\nu} + \Delta \mathbf{M}_{\mu\nu}, \tag{13}$$

$$\tilde{\mathbf{M}}_{\mu\nu} = \langle \varphi_\mu | \hat{\mathbf{m}} | \varphi_\nu \rangle, \tag{14}$$

$$\Delta \mathbf{M}_{\mu\nu} = \sum_{aij} \langle \varphi_\mu | \tilde{p}_i^a \rangle \Delta \mathbf{M}_{ij}^a \langle \tilde{p}_j^a | \varphi_\nu \rangle. \tag{15}$$

In the real-space grid mode, the magnetic moment is calculated using Eq. (10). In the LCAO mode, Eq. (12) is used. The matrix elements $\mathbf{M}_{\mu\nu}$ are time-independent and calculated only once before the time propagation.

After a complete time propagation, the recorded $\mathbf{m}(t)$ is transformed to the frequency domain as a postprocessing step according to Eq. (6) at each desired ω value. Then, the rotatory strength is calculated according to Eq. (4).

We note that the presented approach uses length representation, which renders the results dependent on the choice of origin when an incomplete basis set is used.[32] The origin is set to the center of the molecule in the presented calculations. While the implementation has this limitation, it appears to be sufficient for many practical purposes, as discussed for Ag^+-mediated guanine duplex in Sec. III. The reader is suggested to explore a recent detailed investigation on the gauge dependence.[32]

C. Computational methods and parameters

For the calculations in this work, we used the PBE exchange-correlation functional.[44] For the ligand-protected Ag_{78} cluster, we used the GLLB-SC potential[45] in addition, as noted in Sec. III.

The molecules were placed into a rectangular unit cell with 8 Å vacuum extension in each dimension from the edge of the molecule. The real-space grid spacing was chosen as $h = 0.2$ Å and the time step was chosen as $\Delta t = 5$, except a coarser setting of $h = 0.3$ Å and $\Delta t = 10$, as was used in the RT/LCAO mode for the Ag^+-mediated guanine duplex and the ligand-protected Ag_{78} cluster. As demonstrated for the Ag^+-mediated guanine duplex, the propagation is converged with the larger time step, and such a coarser grid is in many cases sufficient for calculating the ECD spectrum in the LCAO mode, where the grid is used to represent only the real-space density and the potential.[37,38]

All spectra presented in this work are Gaussian broadened with $\sigma = 0.2$ eV, except that $\sigma = 0.1$ eV was applied to the photoabsorption

spectrum of the ligand-protected Ag_{78} cluster, as noted in Sec. III. All RT-TDDFT calculations were propagated to $T = 30$ fs, which is sufficient for the used σ values as the damping function $e^{-\frac{\sigma^2}{2}t^2}$ vanishes at the end of the propagation (yielding at $t = T = 30$ fs $\sim 10^{-18}$ and 10^{-5} with $\sigma = 0.2$ and 0.1 eV, respectively). The rotatory strength is presented in units of 10^{-40} erg esu cm G^{-1} eV^{-1} = 10^{-40} cgs eV^{-1}.

Per atom, the electronic configuration of valence electrons is H($1s^1$) O($2s^2 2p^4$), C($2s^2 2p^2$), N($2s^2 2p^3$), S($3s^2 3p^4$), P($3s^2 3p^3$), F($2s^2 2p^5$), and Ag($4d^{10} 5s^1$). The remaining electrons were treated as a frozen core. The default PAW dataset package 0.9.20000 was used for all the atoms.

In the LCAO mode, the default GPAW double-zeta polarized (dzp) basis sets[38] were used for all elements, unless otherwise mentioned. For Ag, we used the optimized double-zeta basis set (so-called the "p-valence" basis set) instead. In this basis set, the default *p*-type polarization function is replaced with a bound unoccupied *p*-type orbital and its split-valence complement. The inclusion of 5p orbitals in the basis improves the chemistry and photochemistry, as shown in a previous work.[37]

To test basis set effects in ECD simulations, more complete basis sets were constructed by adding diffuse augmentation functions through truncated numerical Gaussian-type orbitals (NGTOs) to the default dzp basis sets.[46] We denote these basis sets as dzp+NGTOs. Our approach follows a recent study of introducing augmentation functions that demonstrated good results for the Bethe–Salpeter equation (BSE) and LR-TDDFT calculations for molecules with numeric atom-centered orbitals.[47] Gaussian basis function exponential parameters, the ζ-parameters, were taken from aug-cc-pvdz basis sets tabulated in Basis Set Exchange.[48,49] The parameters are tabulated in supplementary material, Table S1.

For comparison, we also calculated the ECD spectrum with the existing LR-TDDFT code in GPAW. The LR-TDDFT approach of GPAW requires a cutoff for the Kohn–Sham single-particle excitations and diagonalizes the Casida matrix; hence, there exists a cut-off parameter in these calculations. We chose a high cut-off energy (>20 eV) to compare with our RT-TDDFT results in this work. The effect of the cutoff to the convergence of LR-TDDFT is discussed in supplementary material, Note S2.

The reported computational run times are obtained with Intel Xeon Gold 6230 processors with Mellanox HDR InfiniBand interconnect as installed in the Puhti supercomputer at CSC–Finnish IT Center for Science.

III. RESULTS

In this section, we present four test cases for our implementation. First, we use a benchmark molecule (*R*)-methyloxirane to validate that our RT-TDDFT implementation can produce the same ECD spectra as the LR-TDDFT implementation in both LCAO and the real-space grid mode. Then, we use a chiral Ag_4 string and a Ag^+-mediated guanine duplex $G_2 - Ag_2^{2+} - G_2$ structure[16,50] to demonstrate that LCAO RT-TDDFT adequately reproduces the rotatory strength of the reference grid mode calculated up to 8 eV. Finally, we apply the LCAO RT-TDDFT approach to a hybrid silver cluster $[Ag_{78}(S\text{-BDPP})_6(SR)_{42}]$ (hereafter denoted as Ag_{78}), where BDPP = 2,4-bis-(diphenylphosphino)pentane and SR = $SPhCF_3$.[42] Ag_{78} is considered to be a large system for TDDFT simulations. We will show that LCAO RT-TDDFT is computationally efficient and produces ECD spectra that compare well with experimental results.

A. (*R*)-methyloxirane

(*R*)-methyloxirane is one of the most typical benchmarks for optical activity calculations.[30,32] Therefore, we choose this chiral molecule as our first test system. The atomic structure is taken from the NIST database. The structure was optimized with the configuration interaction singles–doubles (CISD) method and a 6-31G* Gaussian orbital basis set.[51]

The ECD spectrum of (*R*)-methyloxirane was calculated both with our RT-TDDFT implementation and LR-TDDFT. The dzp+NGTO basis set was used in the LCAO simulations. The RT-TDDFT spectra look identical to the LR-TDDFT ones in both LCAO and the real-space grid mode (the ECD is shown separately for LCAO and real-space grid cases in supplementary material, Fig. S1). The maximum difference is less than 0.5 in cgs units. The dzp+NGTO accurately predicts the four first peaks in comparison to the real-space grid calculation, as shown in Fig. 1, but the dzp basis does not give accurate results in this case (supplementary material, Fig. S2).

B. Ag_4 string

To test our implementation on metallic systems, we use a chiral silver string as the second example. This artificial Ag_4 string has a bond length of 2.7 Å, an Ag–Ag–Ag angle of 150°, and a torsion angle of 10°, as shown in the inset of Fig. 2.

Figures 2(a) and 2(b) show that our RT-TDDFT implementation again successfully reproduces the rotatory strength of LR-TDDFT both in the LCAO and grid mode. The slight disagreement of LR-TDDFT and RT-TDDFT in the grid mode above 4 eV is due to a difficult LR-TDDFT convergence, which is discussed more in detail in supplementary material, Note S2.

Figure 2(c) shows that LCAO again adequately reproduces the rotatory strength from the more accurate grid mode up to 8 eV, which is higher than energies commonly used for recording experimental spectra.

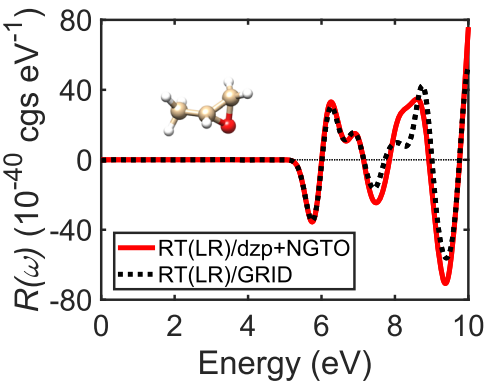

FIG. 1. Rotatory strength of (*R*)-methyloxirane calculated by RT-TDDFT and LR-TDDFT in both LCAO and real-space grid modes.

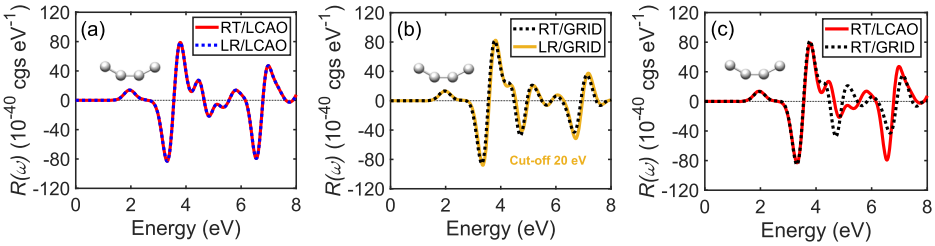

FIG. 2. Rotatory strength of an Ag_4-string (insets) calculated with (a) the LCAO mode and (b) the grid mode. (c) Comparison between the two modes.

C. Ag^+-mediated guanine duplex

After testing on a molecule and a silver string, we apply our method to an organic–metal hybrid system. We use one configuration of the Ag^+-mediated guanine duplex [$G_2 - Ag_2^{2+} - G_2$, Fig. 3(a)], from our previous work.[16] The purpose here is to benchmark the accuracy of the LCAO method for a more complex system.

Comparing the results calculated with the two modes in Fig. 3(b), we find that the dzp basis set reproduces the rotatory strength up to 6 eV, covering the energy window of most experimentally measured ECD spectra. The dzp+NGTO basis improves the agreement up to 8 eV, as shown in supplementary material, Fig. S3.

The system $G_2 - Ag_2^{2+} - G_2$ was also used to evaluate the origin dependence of the current implementation. The origin dependence does not cause severe deviation in the ECD spectra, as shown in supplementary material, Fig. S4. Even the origin displaced by 15 Å away from the center of molecule results only in a moderate difference around 7.0 eV. Previous studies have shown that the origin dependence in the length gauge is mainly due to the non-local pseudopotential and incomplete basis set.[30,32] However, within the PAW method used in the present work, all operators are formally all-electron operators (at least up to the completeness of the partial wave basis). Thus, the origin dependence is expected to be mainly due to incompleteness of the LCAO and partial wave bases.

The benefit of the LCAO mode is its low computational cost. For this system, the LCAO propagation requires less than 10% of the computational resources of the real-space-grid propagation (9 h on 80 cores vs 40 h on 240 cores). Furthermore, we calculated the ECD spectrum using the LCAO mode with a coarser grid parameter h = 0.3 Å and a larger time step of 10 as. The ECD spectrum lies on top of the one obtained from previous RT/LCAO, as shown in Fig. 3(b). The time propagations with coarser parameters took only about 2 h using 80 cores, which is about 50 times faster than the grid mode.

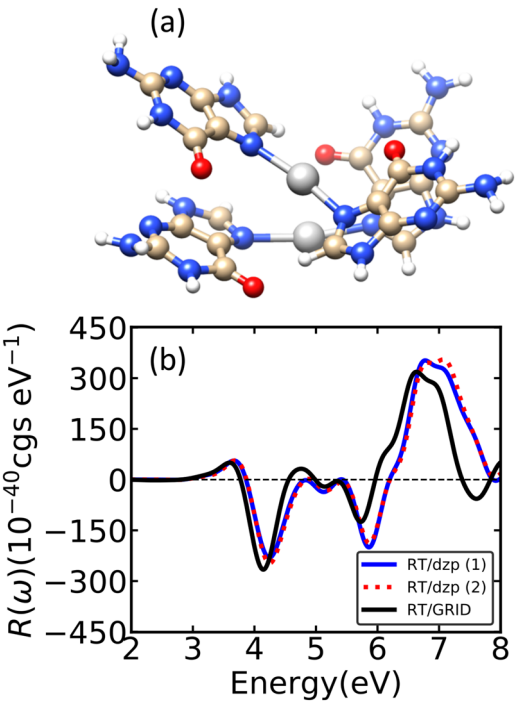

FIG. 3. (a) Structure and (b) rotatory strength of $G_2 - Ag_2^{2+} - G_2$. LCAO calculations use dzp basis sets for the organic part. Here, (1) denotes calculation with grid parameter h = 0.2 Å and time step Δt = 5 as and (2) denotes calculation with coarser grid parameter h = 0.3 Å and time step Δt = 10 as.

D. Ligand-protected Ag_{78} cluster

Next, we illustrate the efficiency and accuracy of our RT-TDDFT/LCAO methodology on a ligand-protected Ag_{78} cluster [Fig. 4(a)] and present a comparison between the experimentally measured[42] and the calculated ECD spectra. We used the x-ray structure reported in Ref. 42 in our calculations [Fig. 4(a)]. The cluster has an Ag_{22} kernel encapsulated in an Ag_{44} shell. Together they form the Ag_{66} core of the cluster [Fig. 4(b)]. Each of the three vertical edges of the Ag_{66} core is capped by a complex $Ag_4(DPPP)_2(SPhCF_3)_8^{4-}$, and each of the three rectangular faces of the trigonal prism is capped by

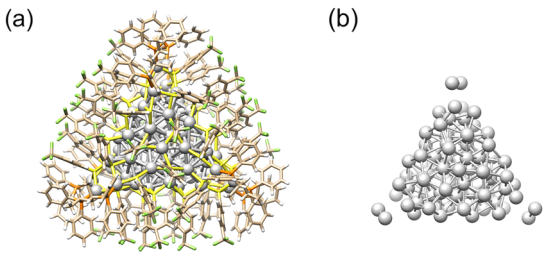

FIG. 4. (a) The structure of the ligand-protected Ag_{78} cluster. Ligand atoms: H, white; C, beige; F, green; P, orange; and S, yellow. (b) Ag atoms in the cluster. The Ag_{66} core atoms are in silver; other Ag atoms are in cyan.

four [$SPhCF_3$] moieties. The total number of atoms is 1074 and the number of valence electrons is 4272. The large size and the complexity of the cluster make it an ideal system to test the computational efficiency of the RT-TDDFT/LCAO approach.

In addition to the PBE exchange–correlation functional, we also used the GLLB-SC exchange–correlation potential.[45] The GLLB-SC functional was chosen because earlier studies show that it provides more accurate predictions of the optical absorption spectra of Ag clusters in comparison to both the local density approximation (LDA) and generalized gradient approximations (GGA).[37]

For the Ag_{78} cluster, we have also calculated the photoabsorption spectrum [Fig. 5(a)]. Both GLLB-SC and PBE reproduce the first peak of the measured absorption spectrum. However, the GLLB-SC spectrum is red-shifted by 0.14 eV and PBE is red-shifted by 0.28 eV.

Table I and Fig. 5(b) present the comparison between the experimentally measured[42] and the calculated ECD spectra. The TDDFT spectra are shifted to higher energies by the same amount as the optical spectra in Fig. 5(a). Both the PBE and GLLB-SC functional capture the main features of the experimental ECD, which are the four positive peaks (a, c, e, and f) and the two negative peaks (b and d).

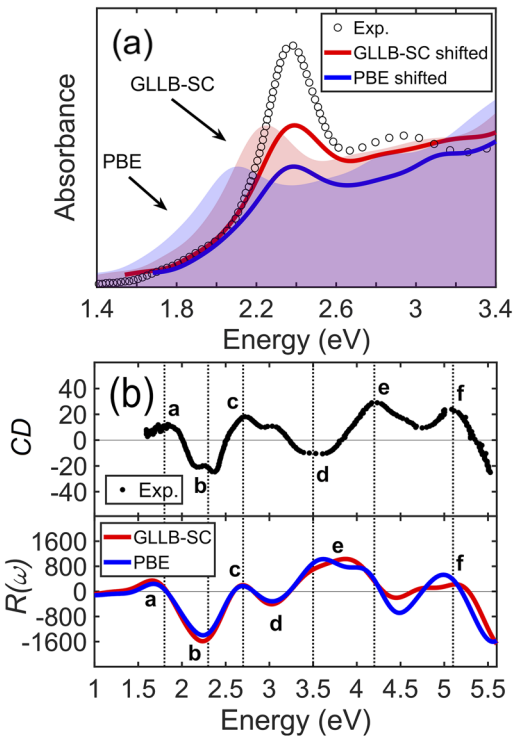

FIG. 5. (a) Photoabsorption spectrum of Ag_{78}. Shaded areas represent calculated spectra and line shifted calculated spectra. The GLLB-SC spectrum was shifted by 0.14 eV and the PBE spectrum was shifted by 0.28 eV. Gaussian broadening with σ = 0.1 eV was applied. (b) The experimental (top panel) and calculated (lower panel) ECD spectra of Ag_{78}. Default dzp basis sets were used for other than Ag atoms. Gaussian broadening with σ = 0.2 eV was applied to approximately match the spectral linewidth with the experimental data. The calculated ECD spectra were shifted according to the shifts done for calculated absorption spectra.

TABLE I. The ECD peak positions in Fig. 5 (in units of eV). The calculated peak positions are shifted as in Fig. 5.

Peak	Expt.	PBE	GLLB-SC
a	1.8	1.68	1.67
b	2.3	2.23	2.27
c	2.7	2.69	2.69
d	3.5	3.04	3.03
e	4.2	3.83	3.79
f	5.1	4.99	5.14

We now briefly discuss the differences between the theoretical spectra and the experimental spectrum. The calculated absorption and ECD spectra are shifted to lower energies likely due to the underestimation of the energy gap between occupied and unoccupied KS states in the DFT simulations and mismatches in the Ag d-band location. The underestimation is less pronounced in the GLLB-SC calculations because GLLB-SC introduces an orbital-energy dependent localization of the exchange hole and describes Ag d-orbitals more accurately. However, the improved description of the energy gap in GLLB-SC does not remove the mismatch of peaks d and e, suggesting that there may be transitions that need a better description. Furthermore, the ECD spectrum was measured in a solvent. The fact that our calculations are performed for the experimental crystal x-ray structure and without conformational sampling may contribute to the differences. Using the larger dzp+NGTO basis set does not remove these differences, as demonstrated in supplementary material, Fig. S5.

The origin of the chirality of nanoclusters is broadly classified into three categories: (1) intrinsic chirality of the metal core, (2) the chiral arrangement of the achiral surface structure, and (3) extrinsic chirality induced by homochiral ligands.[52] To better understand the chiroptical properties of the cluster, we also calculated the ECD of the Ag_{22} and Ag_{66} core of the cluster by the LCAO/RT-TDDFT method with the same parameters as the full cluster. The PBE functional was used in these calculations. The results are shown in Fig. 6. From Fig. 6, we can conclude that the cluster is entirely chiral because even the inner Ag_{22} core exhibits an ECD signal. Ag_{66} and the full cluster have similar intensities of the CD signal, but the

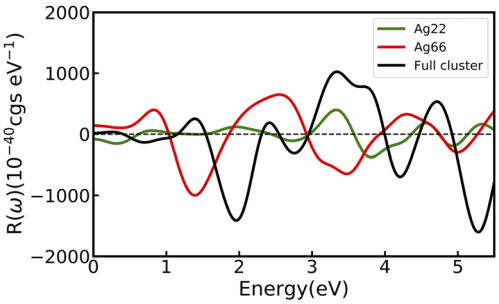

FIG. 6. Rotatory strength of Ag_{22}, Ag_{66}, and the full ligand-protected Ag_{78} cluster. No spectrum is shifted.

peak positions are different, indicating that both the Ag core and the ligand layer play an essential role for the CD signal of the cluster.

The ECD calculation of the ligand protected Ag_{78} cluster took 24 h with 200 cores with the PBE exchange–correlation functional and took 33 h with the GLLB-SC functional. This is remarkably fast for TDDFT ECD calculations of such a large system.

IV. CONCLUSIONS

We presented a RT-TDDFT implementation for calculating ECD in the GPAW package, which supports both the LCAO mode and grid mode. While RT-TDDFT/LCAO is less accurate than RT-TDDFT/GRID, our tests have shown that the LCAO method nevertheless produces matching spectra in the experimentally relevant energy ranges. More complete basis sets improve the agreement with the grid mode in most test cases, but for the high energy region where the transitions are ionizing, the plane waves are, in principle, required.

The high computational efficiency of the RT-TDDFT/LCAO is enabled by the combination of localized orbitals and the PAW method. We demonstrated the efficiency of this code by computing the ECD spectra of a large hybrid nanocluster with 1000 atoms, a system whose ECD is challenging to compute by RT-TDDFT/GRID or conventional linear-response formalisms.

Our RT-TDDFT implementation with localized orbitals and PAW in GPAW opens the door to study the large-scale chiral systems with good accuracy and efficiency. We expect that our open-source implementation will be advantageous for studying the chiroptical property of large systems without excessive computational cost. For example, plasmonic clusters with a selected size and shape may significantly enhance the ECD of chiral molecules, which have potential as chirality sensors.[53]

SUPPLEMENTARY MATERIAL

See the supplementary material for Fig. S1: comparison of LR-TDDFT and RT-TDDFT for R-methyloxirane; Figs. S2, S3, and S5: the effect of diffuse functions for different test cases; Fig. S4: the effect of shifting the origin of the magnetic moment calculation; Fig. S6: convergence of LR-TDDFT calculations with respect to the cut-off energy; Table S1: parameters for diffuse functions; Note S1: derivation of the magnetic moment from the optical rotatory tensor; and Note S2: convergence of LR-TDDFT calculations with respect to the cut-off energy.

ACKNOWLEDGMENTS

This work was supported by the Academy of Finland under Grant Nos. 279240, 295602, 308647, 312556, 314298, and 332429. T.P.R. also acknowledges support from the European Union's Horizon 2020 research and innovation programme under Marie Skłodowska-Curie Grant Agreement No. 838996. We acknowledge computational resources provided by the CSC–IT Center for Science (Finland), the Aalto Science-IT project, and the Swedish National Infrastructure for Computing (SNIC) at PDC (Stockholm).

DATA AVAILABILITY

The data that support the findings of this study are openly available at http://doi.org/10.5281/zenodo.4300008.

REFERENCES

[1] L. D. Barron, "Chirality and life," Space Sci. Rev. **135**, 187–201 (2008).
[2] E. Tokunaga, T. Yamamoto, E. Ito, and N. Shibata, "Understanding the thalidomide chirality in biological processes by the self-disproportionation of enantiomers," Sci. Rep. **8**, 17131 (2018).
[3] A. L. Spek, "Absolute structure determination: Pushing the limits," Acta Crystallogr., Sect. B **72**, 659–660 (2016).
[4] W. A. Nugent, T. V. RajanBabu, and M. J. Burk, "Beyond nature's chiral pool: Enantioselective catalysis in industry," Science **259**, 479–483 (1993).
[5] T. J. Davis and D. E. Gómez, "Interaction of localized surface plasmons with chiral molecules," Phys. Rev. B **90**, 235424 (2014).
[6] C. Gautier and T. Bürgi, "Chiral gold nanoparticles," ChemPhysChem **10**, 483–492 (2009).
[7] J. R. Sanchez-Valencia, T. Dienel, O. Gröning, I. Shorubalko, A. Mueller, M. Jansen, K. Amsharov, P. Ruffieux, and R. Fasel, "Controlled synthesis of single-chirality carbon nanotubes," Nature **512**, 61–64 (2014).
[8] M. Bode, M. Heide, K. von Bergmann, P. Ferriani, S. Heinze, G. Bihlmayer, A. Kubetzka, O. Pietzsch, S. Blügel, and R. Wiesendanger, "Chiral magnetic order at surfaces driven by inversion asymmetry," Nature **447**, 190–193 (2007).
[9] C. Noguez and I. L. Garzón, "Optically active metal nanoparticles," Chem. Soc. Rev. **38**, 757–771 (2009).
[10] S. Knoppe and T. Bürgi, "Chirality in thiolate-protected gold clusters," Acc. Chem. Res. **47**, 1318–1326 (2014).
[11] D. Zerrouki, J. Baudry, D. Pine, P. Chaikin, and J. Bibette, "Chiral colloidal clusters," Nature **455**, 380–382 (2008).
[12] H.-E. Lee, H.-Y. Ahn, J. Mun, Y. Y. Lee, M. Kim, N. H. Cho, K. Chang, W. S. Kim, J. Rho, and K. T. Nam, "Amino-acid- and peptide-directed synthesis of chiral plasmonic gold nanoparticles," Nature **556**, 360–365 (2018).
[13] J. T. A. Jones, T. Hasell, X. Wu, J. Bacsa, K. E. Jelfs, M. Schmidtmann, S. Y. Chong, D. J. Adams, A. Trewin, F. Schiffman, F. Cora, B. Slater, A. Steiner, G. M. Day, and A. I. Cooper, "Modular and predictable assembly of porous organic molecular crystals," Nature **474**, 367–371 (2011).
[14] J. Kypr, I. Kejnovská, D. Renciuk, and M. Vorlickova, "Circular dichroism and conformational polymorphism of DNA," Nucleic Acids Res. **37**, 1713–1725 (2009).
[15] L. Chang, O. Baseggio, L. Sementa, D. Cheng, G. Fronzoni, D. Toffoli, E. Aprà, M. Stener, and A. Fortunelli, "Individual component map of rotatory strength and rotatory strength density plots as analysis tools of circular dichroism spectra of complex systems," J. Chem. Theory Comput. **14**, 3703–3714 (2018).
[16] X. Chen, E. Makkonen, D. Golze, and O. Lopez-Acevedo, "Silver-stabilized guanine duplex: Structural and optical properties," J. Phys. Chem. Lett. **9**, 4789–4794 (2018).
[17] L. A. Espinosa Leal, A. Karpenko, S. Swasey, E. G. Gwinn, V. Rojas-Cervellera, C. Rovira, and O. Lopez-Acevedo, "The role of hydrogen bonds in the stabilization of silver-mediated cytosine tetramers," J. Phys. Chem. Lett. **6**, 4061–4066 (2015).
[18] T. D. Crawford, "*Ab initio* calculation of molecular chiroptical properties," Theor. Chem. Acc. **115**, 227–245 (2006).
[19] E. Runge and E. K. U. Gross, "Density-functional theory for time-dependent systems," Phys. Rev. Lett. **52**, 997–1000 (1984).
[20] C. Diedrich and S. Grimme, "Systematic investigation of modern quantum chemical methods to predict electronic circular dichroism spectra," J. Phys. Chem. A **107**, 2524–2539 (2003).
[21] J. Autschbach, T. Ziegler, S. J. A. van Gisbergen, and E. J. Baerends, "Chiroptical properties from time-dependent density functional theory. I. Circular dichroism spectra of organic molecules," J. Chem. Phys. **116**, 6930–6940 (2002).
[22] M. E. Casida, "Time-dependent density functional response theory for molecules," in *Recent Advances in Density Functional Methods, Part I*, edited by D. P. Chong (World Scientific, Singapore, 1995), p. 155.

[23]M. R. Provorse and C. M. Isborn, "Electron dynamics with real-time time-dependent density functional theory," Int. J. Quantum Chem. **116**, 739–749 (2016).
[24]M. Petersilka, U. J. Gossmann, and E. K. U. Gross, "Excitation energies from time-dependent density-functional theory," Phys. Rev. Lett. **76**, 1212–1215 (1996).
[25]M. E. Casida, "Time-dependent density-functional theory for molecules and molecular solids," J. Mol. Struct.: THEOCHEM **914**, 3–18 (2009).
[26]K. Yabana and G. F. Bertsch, "Time-dependent local-density approximation in real time," Phys. Rev. B **54**, 4484–4487 (1996).
[27]K. Yabana and G. F. Bertsch, "Application of the time-dependent local density approximation to optical activity," Phys. Rev. A **60**, 1271–1279 (1999).
[28]J. J. Goings, P. J. Lestrange, and X. Li, "Real-time time-dependent electronic structure theory," Wiley Interdiscip. Rev.: Comput. Mol. Sci. **8**, e1341 (2018).
[29]S. Tussupbayev, N. Govind, K. Lopata, and C. J. Cramer, "Comparison of real-time and linear-response time-dependent density functional theories for molecular chromophores ranging from sparse to high densities of states," J. Chem. Theory Comput. **11**, 1102–1109 (2015).
[30]D. Varsano, L. A. Espinosa-Leal, X. Andrade, M. A. L. Marques, R. di Felice, and A. Rubio, "Towards a gauge invariant method for molecular chiroptical properties in TDDFT," Phys. Chem. Chem. Phys. **11**, 4481–4489 (2009).
[31]J. J. Goings and X. Li, "An atomic orbital based real-time time-dependent density functional theory for computing electronic circular dichroism band spectra," J. Chem. Phys. **144**, 234102 (2016).
[32]J. Mattiat and S. Luber, "Electronic circular dichroism with real time time dependent density functional theory: Propagator formalism and gauge dependence," Chem. Phys. **527**, 110464 (2019).
[33]S. Sun, R. A. Beck, D. Williams-Young, and X. Li, "Simulating magnetic circular dichroism spectra with real-time time-dependent density functional theory in gauge including atomic orbitals," J. Chem. Theory Comput. **15**, 6824–6831 (2019).
[34]D. B. Williams-Young, A. Petrone, S. Sun, T. F. Stetina, P. Lestrange, C. E. Hoyer, D. R. Nascimento, L. Koulias, A. Wildman, J. Kasper, J. J. Goings, F. Ding, A. E. DePrince III, E. F. Valeev, and X. Li, "The chronus quantum software package," Wiley Interdiscip. Rev.: Comput. Mol. Sci. **10**, e1436 (2020).
[35]J. J. Mortensen, L. B. Hansen, and K. W. Jacobsen, "Real-space grid implementation of the projector augmented wave method," Phys. Rev. B **71**, 035109 (2005).
[36]J. Enkovaara, C. Rostgaard, J. J. Mortensen, J. Chen, M. Dułak, L. Ferrighi, J. Gavnholt, C. Glinsvad, V. Haikola, H. A. Hansen *et al.*, "Electronic structure calculations with GPAW: A real-space implementation of the projector augmented-wave method," J. Phys.: Condens. Matter **22**, 253202 (2010).
[37]M. Kuisma, A. Sakko, T. P. Rossi, A. H. Larsen, J. Enkovaara, L. Lehtovaara, and T. T. Rantala, "Localized surface plasmon resonance in silver nanoparticles: Atomistic first-principles time-dependent density-functional theory calculations," Phys. Rev. B **91**, 115431 (2015).
[38]A. H. Larsen, M. Vanin, J. J. Mortensen, K. S. Thygesen, and K. W. Jacobsen, "Localized atomic basis set in the projector augmented wave method," Phys. Rev. B **80**, 195112 (2009).
[39]P. E. Blöchl, "Projector augmented-wave method," Phys. Rev. B **50**, 17953–17979 (1994).
[40]M. Walter, H. Häkkinen, L. Lehtovaara, M. Puska, J. Enkovaara, C. Rostgaard, and J. J. Mortensen, "Time-dependent density-functional theory in the projector augmented-wave method," J. Chem. Phys. **128**, 244101 (2008).
[41]T. P. Rossi, M. Kuisma, M. J. Puska, R. M. Nieminen, and P. Erhart, "Kohn–sham decomposition in real-time time-dependent density-functional theory: An efficient tool for analyzing plasmonic excitations," J. Chem. Theory Comput. **13**, 4779–4790 (2017).
[42]H. Yang, J. Yan, Y. Wang, G. Deng, H. Su, X. Zhao, C. Xu, B. K. Teo, and N. Zheng, "From racemic metal nanoparticles to optically pure enantiomers in one pot," J. Am. Chem. Soc. **139**, 16113–16116 (2017).
[43]T. Bondo Pedersen and A. E. Hansen, "*Ab initio* calculation and display of the rotary strength tensor in the random phase approximation. Method and model studies," Chem. Phys. Lett. **246**, 1–8 (1995).
[44]J. P. Perdew, K. Burke, and M. Ernzerhof, "Generalized gradient approximation made simple," Phys. Rev. Lett. **77**, 3865–3868 (1996).
[45]M. Kuisma, J. Ojanen, J. Enkovaara, and T. Rantala, "Kohn–Sham potential with discontinuity for band gap materials," Phys. Rev. B **82**, 115106 (2010).
[46]T. P. Rossi, S. Lehtola, A. Sakko, M. J. Puska, and R. M. Nieminen, "Nanoplasmonics simulations at the basis set limit through completeness-optimized, local numerical basis sets," J. Chem. Phys. **142**, 094114 (2015).
[47]C. Liu, J. Kloppenburg, Y. Yao, X. Ren, H. Appel, Y. Kanai, and V. Blum, "All-electron *ab initio* Bethe–Salpeter equation approach to neutral excitations in molecules with numeric atom-centered orbitals," J. Chem. Phys. **152**, 044105 (2020).
[48]K. L. Schuchardt, B. T. Didier, T. Elsethagen, L. Sun, V. Gurumoorthi, J. Chase, J. Li, and T. L. Windus, "Basis set exchange: A community database for computational sciences," J. Chem. Inf. Model. **47**, 1045–1052 (2007).
[49]B. P. Pritchard, D. Altarawy, B. Didier, T. D. Gibson, and T. L. Windus, "New basis set exchange: An open, up-to-date resource for the molecular sciences community," J. Chem. Inf. Model. **59**, 4814–4820 (2019).
[50]E. Makkonen, P. Rinke, O. Lopez-Acevedo, and X. Chen, "Optical properties of silver-mediated DNA from molecular dynamics and time dependent density functional theory," Int. J. Mol. Sci. **19**, 2346 (2018).
[51]National Institute of Standards and Technology, computational chemistry comparison and benchmark DataBase, Release 20. CISD/6-31G* calculated geometry for C_3H_6O (propylene oxide) $^1A\ C_1$.
[52]Y. Li, T. Higaki, X. Du, and R. Jin, "Chirality and surface bonding correlation in atomically precise metal nanoclusters," Adv. Mater. **32**, 1905488 (2020).
[53]A. Ben-Moshe, B. M. Maoz, A. O. Govorov, and G. Markovich, "Chirality and chiroptical effects in inorganic nanocrystal systems with plasmon and exciton resonances," Chem. Soc. Rev. **42**, 7028–7041 (2013).